Journal of Energy Storage 117 (2025) 116121

Contents lists available at ScienceDirect

Journal of Energy Storage

journal homepage: www.elsevier.com/locate/est

Research Papers

Computational and experimental analysis of a novel triply periodic minimal surface heat sink with phase change material

Mohammad Arqam [a,*], Laryssa Sueza Raffa [a], Simone Spisiak [a], Lee Clemon [a], Zhen Luo [a], Matt Ryall [b], Mohammad S. Islam [a], Nick S. Bennett [a]

[a] School of Mechanical and Mechatronic Engineering, University of Technology Sydney, Ultimo, NSW 2007, Australia
[b] Mawson Rovers, Eveleigh, NSW 2015, Australia

ARTICLE INFO

Keywords:
Triply periodic minimal surface (TPMS)
Phase change material (PCM)
Thermal conductivity enhancer (TCE)
Thermal management
Electronics

ABSTRACT

The rapid miniaturization of modern electronics has led to significant overheating issues, which pose substantial risks to their performance, reliability, and service life. This study aims to address these challenges by proposing a novel heat sink design incorporating Triply Periodic Minimal Surface (TPMS)-based metal lattice structures embedded with a phase change material (PCM). A comprehensive numerical and experimental investigation was conducted on a 3D-printed PCM metal-lattice heat sink. By employing a three-dimensional unsteady numerical approach and the finite volume method, this study evaluated the metal lattice as a thermal conductivity enhancer. A parametric study was performed to assess the impacts of the heater power input, material, design, and applied heat flux direction. The tested materials were Stainless Steel (SS) and titanium (Ti), with paraffin wax as the PCM. The findings demonstrated that the TPMS-based lattice structure (P3) helps improve the heat exchange between the metal and PCM by facilitating gradual and uniform melting within the system. The SS (P3) heat sink showed up to a 9 % reduction in base temperature compared to Ti (P3) under heater power inputs ranging from 5.1 W to 8.6 W, attributed to its better thermal conductivity. The parametric analysis indicated that, when compared to radial fin design (P5) under multidirectional heat input, P5 returns 3 to 4 °C lower base temperature than P3 for SS and Ti under base-only heating case scenario. On the contrary, P3 outperformed P5 by maintaining side walls 6 to 8 °C cooler during side-only heating. However, the combined effect of base and side heating was found to be insignificant for both designs. The analysis concluded that although the radial fin design (P5) performs slightly better under base-only heating conditions, the TPMS design (P3) would otherwise outperform it, particularly in applications involving multi-directional heat input.

1. Introduction

Efficient thermal management is crucial to address the thermal challenges associated with modern electronics. Stabilizing temperatures to the desired levels is essential for ensuring performance, reliability, durability, and component safety. As electronics become more compact and demand higher power, dissipating excess heat becomes critical to prevent operational failures. Nearly 50 % of electronic failures can be attributed to elevated temperatures [1]. Phase change materials (PCMs) have attracted significant attention owing to their appealing thermophysical properties, especially their high latent heat of fusion. Recent reviews [1,2] have discussed the use of PCMs in electronic cooling across various temperature ranges. Although PCMs offer several benefits, they are typically not employed independently owing to their low thermal conductivities. To circumvent this challenge, they are commonly combined with thermal conductivity enhancers (TCEs), such as fins [3–5], metal fibres [7,8,19], encapsulated PCM [9], metal foams [6,10–12], nanoparticles [13–18] and graphitic matrices [20–23].

The recent surge in the adoption of additive manufacturing (AM) techniques has redirected research efforts towards employing architected metal lattices as thermal energy storage (TESs) for phase change materials (PCMs). AM enables the production of intricate geometries that are not possible using other manufacturing methods, thereby facilitating the analysis of metal lattices with complex topologies for TES applications. Several studies have been conducted in which metal lattices embedded with PCM were used for TES. The research conducted by Ho et al. [23] developed a paraffin wax-based tree-like heat-sink geometry. The researchers assessed the impact of various paraffin wax impregnation levels and analyzed the temperature distribution and heat

* Corresponding author.
E-mail address: Mohammad.Arqam@uts.edu.au (M. Arqam).

https://doi.org/10.1016/j.est.2025.116121
Received 19 September 2024; Received in revised form 17 February 2025; Accepted 6 March 2025
Available online 11 March 2025

Nomenclature

FVM	Finite volume method
PCM	Phase change material
TCE	Thermal conductivity enhancer
TM	Thermal Management
HTC	Heat transfer coefficient, W/m^{2}K
TEC	Thermal energy storage
CAD	Computer aided design
AM	Additive manufacturing
TPMS	Triply periodic minimal surface
SS	Stainless steel
Ti	Titanium
HP	Heater power
M	Million
C	Mush constant
c_p	Specific heat capacity, J/KgK
ρ	Density, Kg/m^3
g	Gravitational acceleration, m/s^2
H	Height, mm
k	Thermal conductivity, W/mK
L	Latent heat of fusion, J/KgK
m	Mass, kg
p	Pressure, Pa
u	Velocity component in x direction, m/s
v	Velocity component in y direction, m/s
w	Velocity component in z direction, m/s
S	Source term in momentum eq.
3D	Three dimensional
W	Width, mm
t	Time, s
t_{fin}	Fin thickness, mm
t_{base}	Base thickness, mm
t_{wall}	Wall thickness, mm
T_{sol}	PCM solid temperature, °C
T_{liq}	PCM liquid temperature, °C
Q	Power input, W

Subscripts

ini	Initial
l	Liquid
m	Melting
f	Phase change material (liquid)
ref	Reference
x, y, z	Cartesian coordinates
s	Solid (metal)

Greek

μ	Viscosity, Kg/ms
β	Thermal expansion coefficient, 1/K
λ	Liquid fraction
δ	Arbitrary small value

transfer characteristics. The results revealed that the PCM-based heat sink demonstrated superior thermal performance, as indicated by its ability to maintain a lower base temperature than a fin-structure and plain heat sinks for heat fluxes ranging from 4.00 to 7.24 kW/m^2. Yuandong et al. [24] demonstrated that using an AM lattice-structure heat sink with n-tetradecane PCM in a thermal vacuum chamber simulating space conditions can significantly enhance heat transfer performance. These findings suggest that this heat sink may provide thermal management solutions for space applications. The printed metal lattice heat sink was found to have an equivalent thermal conductivity 13 times higher than that of PCM. Hu et al. [25] found that the use of AM structured porous materials as PCM-based heat sinks offers a promising solution for efficient thermal management. A study by Righetti et al. [26] demonstrated that incorporating PCM in 3D periodic structures significantly improved the heat transfer performance, for 10–30 W and 10–40 mm pore sizes. The authors of the study by Iradukunda et al. [27] found that using AM topology-optimized heat sinks in conjunction with PCMs outperformed conventional plate fin designs. The findings also highlight the potential of additive manufacturing and PCMs for improving the efficiency of heat sink designs, which could have important implications for a wide range of applications, including electronic cooling.

Recently, there has been a growing interest in the utilization of Triply Periodic Minimal Surfaces (TPMS) for heat transfer applications. This interest is due to the unique properties of TPMS, which allow for efficient heat transfer and improved thermal performance compared to traditional surfaces, making them ideal for a variety of applications, such as thermal management systems, energy efficiency, and heat exchangers. Furthermore, the capability to manufacture TPMS efficiently via AM enables greater flexibility and customization in their design and application. Catchpole-Smith et al. [28] investigated AM TPMS lattices for thermal conductivity and found that the architecture and porosity of these structures have a significant impact on their thermal properties, with certain lattice structures exhibiting superior thermal conductivity compared to others. This highlights the importance of carefully designing and engineering lattice structures for optimal thermal management of additively manufactured TPMS components. Qureshi et al. [29] conducted an experimental study of TPMS lattices with paraffin wax, and their results were consistent with those of previous studies. Sél'o et al. [30] investigated the influence of heat treatment on the anisotropy and thermal conductivity of 3D-printed TPMS lattices and discovered that heat treatment increased thermal conductivity while eliminating anisotropy. Building on prior research, further studies conducted by Qureshi et al. [31] assessed the performance of TPMS-based metal lattices and conventional metal foams under a variety of heat flux conditions. The findings demonstrated that TPMS-based lattice structures outperformed metal foams in both pure conduction and scenarios where liquid PCM buoyancy was considered. Their investigations of sheet-based and solid TPMS lattices incorporating PCM also revealed the potential benefits of these structures in thermal energy storage [32,33]. Qureshi et al. [34] sought to further explore the effects of both functional grading and porosity on the performance of 3D printable TPMS lattices incorporating PCM. By analyzing the results, they found that these factors significantly influenced the thermal response, highlighting the importance of geometric parameters in the design of TES systems.

The above literature suggests that while TPMS structures with PCM have promising applications, their performance under different materials (stainless steel and titanium), heater power inputs, and applied heat flux directions, which are typical of electronic cooling, have not been extensively studied. This study aims to evaluate the feasibility of using TPMS based metal lattice heat sinks with PCM under heat fluxes ranging from 5.1 to 8.6 W. Two heat sink designs, a metal lattice (P3) and a radial fin (P5) as depicted in Fig. 1, were selected due to their contrasting surface areas and liquid PCM flow resistances and analyzed under the influence of multidirectional heat input. P3 has symmetrical metal lattice structure while P5 has radial fins attached to the base. The novelty lies in designing a novel compact TPMS-based metal lattice and radial fin heat sink using AM techniques and developing three-dimensional numerical models that consider phase change material as an energy-storing medium and multidirectional heating. The research began with numerical modelling, followed by experimental validation,

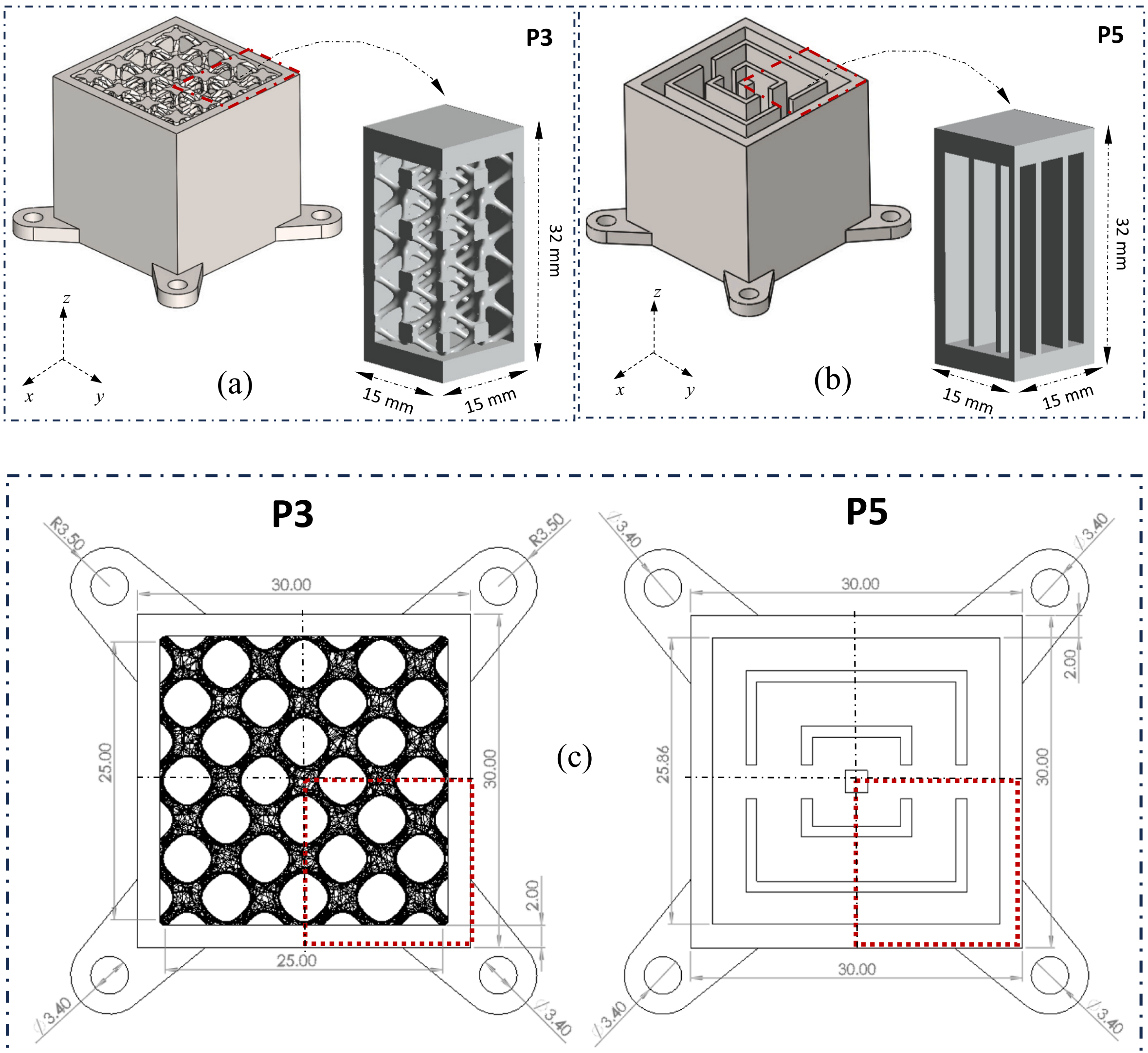

Fig. 1. Schematic diagram of heat sinks (a) CAD model of Design P3; (b) CAD model of Design P5; (c) Dimensions – all in mm.

Table 1
Design of experiments.

Cases	Heat sink model	Material	Power input (W)	HTC (W/m^{2}K)	Heating	Ambient
1 (base)	P3	SS	8.6	40.0	Base	Atmosphere
2	P3	SS	6.8	40.0	Base	Atmosphere
3	P3	SS	5.1	40.0	Base	Atmosphere
4	P3	Ti	8.6	40.0	Base	Atmosphere
5	P3	Ti	6.8	40.0	Base	Atmosphere
6	P3	Ti	5.1	40.0	Base	Atmosphere
7	P5	SS	8.6	40.0	Base	Atmosphere
8	P5	Ti	8.6	40.0	Base	Atmosphere
9	P3	SS	8.6	40.0	Side	Atmosphere
10	P5	SS	8.6	40.0	Side	Atmosphere
11	P3	Ti	8.6	40.0	Side	Atmosphere
12	P5	Ti	8.6	40.0	Side	Atmosphere
13	P3	SS	8.6	40.0	Base+Side	Atmosphere
14	P5	SS	8.6	40.0	Base+Side	Atmosphere
15	P3	Ti	8.6	40.0	Base+Side	Atmosphere
16	P5	Ti	8.6	40.0	Base+Side	Atmosphere

considering possible variable directional heat inputs to assess the design feasibility in terms of thermal performance. The ultimate aim is to provide insights for selecting the best geometry for the efficient cooling of electronics under varying directional heat inputs. This research contributes to decision-making in heat-sink design and development for effective heat dissipation from high-power electronics. Moreover, future recommendations are provided to inform design engineers and researchers who wish to leverage phase change material metal lattice heat sinks for better thermal management of modern electronics.

Table 2
Design parameters for P3 and P5.

Design	H (mm)	t_{base} (mm)	t_{lid} (mm)	t_{wall} (mm)	t_{fin} (mm)	Mass (metal) (gram)	Mass (PCM) (gram)	Total mass (gram)
P3	32	3	3	2	–	27.49	3.19	30.68
P5	32	3	3	2	0.98	27.51	3.20	30.71

Table 3
Thermo-physical properties of materials included in the analysis [35–37].

Materials	Properties							
	Density $\left(\frac{kg}{m^3}\right)$	Specific heat $\left(\frac{J}{kgK}\right)$	Thermal conductivity $\left(\frac{W}{mK}\right)$	Viscosity $\left(\frac{kg}{m.s}\right)$	Thermal expansion coefficient, β $\left(\frac{1}{K}\right)$	Latent heat, L $\left(\frac{J}{kg}\right)$	Solidus temperature (°C)	Liquidus temperature (°C)
Stainless Steel (316-L)	8030	502.5	16.3	–	–	–	–	–
Titanium (Ti-6Al-4 V)	4850	544.25	11.4	–	–	–	–	–
PCM (Paraffin Wax)	880	2000	0.2	0.03	0.00011	170,000	53	58

2. Numerical model

2.1. Design

Two heat sink designs, namely a TPMS-based metal lattice (P3) and radial fins (P5), are considered, with P3 being the main focus of this study. P3 had baseline external dimensions of $30 \times 30 \times 32$ mm^3 and an internal wall thickness of 2 mm (Fig. 1). The design is monolithic, featuring four mounting lugs at the base used to secure the heat sink to a rig for testing, four side lugs for sensor mounting, and two holes on the top face for insertion of a Solid Liquid Phase Change Material (SL-PCM). A level set method was used to generate and optimize the TPMS design (P3), while SolidWorks 2021 was employed to manually produce the radial fin design (P5). The preliminary performance of the designs was simulated using ANSYS-Fluent 2021 R2. Both heat sinks were fabricated using a powder bed fusion additive manufacturing (PBF-AM) process. A GE Concept Laser M2 Series 5 (400 W) was used for printing. This process was selected to support the efficient and accurate manufacturing of the complex geometries. Heat sinks were produced in two materials, Stainless Steel 316 L and Ti-6Al-4 V. A total of 16 cases (Case 1 being the base case) were analyzed based on the material, design, heat input, and direction of the supplied heat flux. The design of experiments is presented in Table 1 with the base case corresponding to the experimental conditions used for validation purposes.

2.1.1. Material

Titanium (Ti-6Al-4 V) and Stainless-Steel 316 L metal material variations of the model were tested and numerically modelled. These materials were selected because of the considerable difference in their thermophysical properties, namely, specific heat, density, and thermal conductivity and are commonly used in PBF-AM to match industry demand. Titanium has lower density and thermal conductivity than stainless steel. This makes it lighter than stainless steel but not as good at conducting heat. By comparison, stainless steel has a lower specific heat than titanium, indicating that less input heat is required to raise the temperature by a unit of mass. Both materials exhibit high corrosion resistance and radiation shielding and are commonly used in latent heat energy storage applications.

2.1.2. Internal structure

As shown in Fig. 1, the P3 design featured an internal lattice structure. This TPMS cellular structure was selected to facilitate better thermal exchange of heat between the PCM and the heat sink. The lattice was designed with smooth surface angles and volume fraction optimized to increase heat transfer effectiveness. The geometry comprised 96 cells, each with a porosity of 85 % and an overall height of 26 mm. Design P5 incorporated four evenly spaced 0.98 mm tick radial fins, along with a 2 mm central pin fin, to enhance unidirectional heat transfer.

2.1.3. Simulation domain

A quarter of the design was sufficient for the numerical analysis owing to its symmetrical properties. Consequently, a simplified geometry with symmetry on two sides, heat flux on one side, and convection on three sides was chosen as the simulation domain. Both the full-sized heat sink and its simplified numerical simulation model are shown in Fig. 1(a) and (b). The design parameters of P3 and P5 are listed in Table 2. The designs were similar in terms of dimensions and weights. The masses listed in Table 2 pertain only to the simulation domain. The total mass of the full-sized heat sink can be estimated by multiplying these numbers by three to account for the remaining three quarters. The actual mass of the heat sink print (P3) used in the experiment was different because of the exclusion of feet, mounting lugs, and the small cavity inside to account for the PCM volume expansion upon melting.

2.2. Numerical procedure

A 3D model of a PCM-based metal lattice heat sink was generated and optimized using a level set method, as illustrated in Fig. 1. The performance of the heat sink was analyzed under various conditions, including different heater power inputs, materials, and heat flux directions, and compared with a radial fin heat sink under multidirectional heating. The simulations were conducted using a pressure-based finite volume method (FVM) in ANSYS Fluent 2021 R2. The simulations employed the PRESTO and PISO algorithms for pressure-velocity coupling, a second-order upwind scheme for convective terms, and a first-order implicit scheme for time discretization. The under-relaxation factors for pressure, velocity, energy, and liquid fraction were set at 0.3, 0.7, 1, and 0.9 for liquid fraction, with residuals set at 10^{-4} for continuity and momentum, and 10^{-6} for energy equations. The physical dimensions of the model were derived from the design, assuming uniform material properties. The liquid PCM flow in the cavity was assumed laminar, Newtonian, and incompressible. The thermophysical properties of the stainless steel, titanium, and PCM were assumed to be constant. The mushy zone characterized the melting interface, with the Boussinesq approximation accounting for buoyancy effects. The metal was assumed to remain solid, absorbing only sensible heat. PCM volumetric expansion during phase transition and radiative heat transfer has been neglected [31–34]. The thermal resistance between the heater chip and the heat sink base was also ignored. Thermophysical properties of the materials are listed in Table 3.

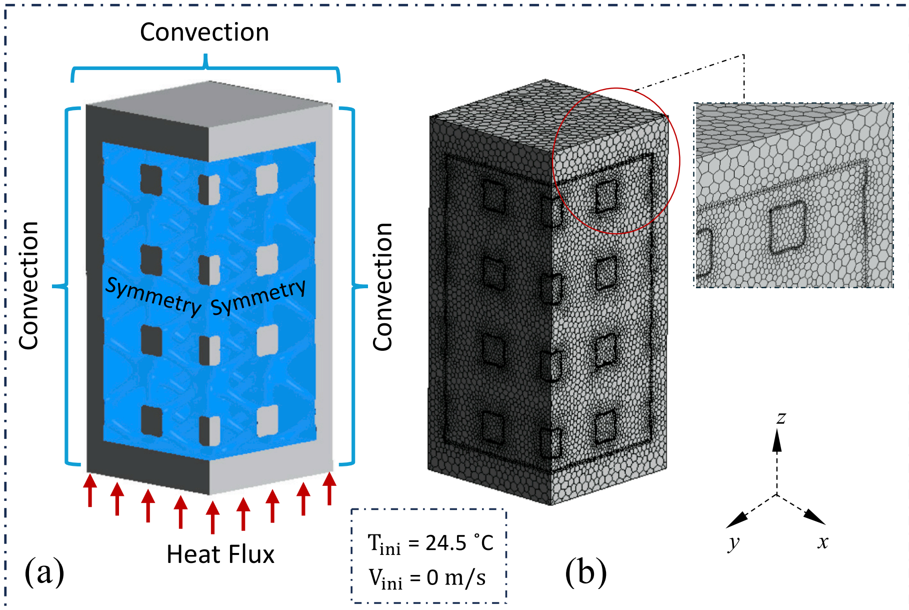

Fig. 2. (a) Initial and boundary conditions; (b) computational grid.

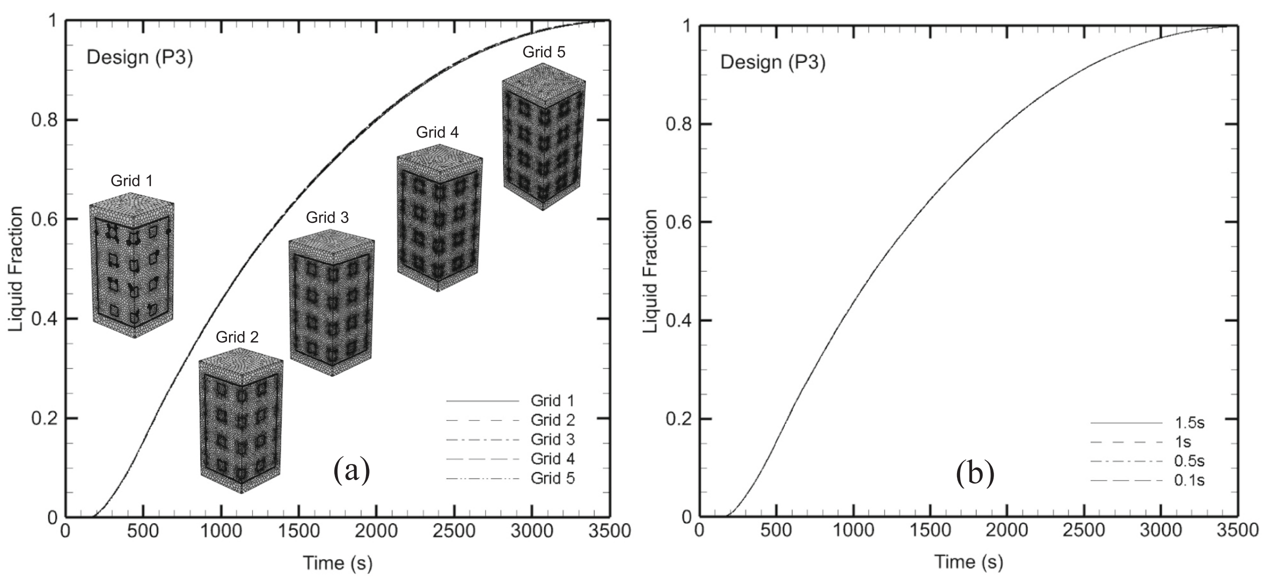

Fig. 3. Stainless steel design P3 liquid fraction (a) grid independence; (b) time step sensitivity.

Table 4
Summary of grid independence analysis.

Grid system	No. of cell	Melting time (s)	Deviation (%)	Base temp (°C)	Deviation (%)
Grid 1	478 K	3472	0.00	91.17	0.00
Grid 2	1.3 M	3476	0.08	91.07	0.10
Grid 3	2.1 M	3479	0.03	91.02	0.05
Grid 4	3.6 M	3481	0.02	90.97	0.05
Grid 5	6.9 M	3484	0.03	90.92	0.05

2.3. Governing equations

The governing equations (continuity, momentum, and energy) for numerical analysis are as follows [38–41]:

Continuity equation:

$$\nabla.\mathbf{u} = 0 \tag{1}$$

Momentum equation:

$$\rho_f\left(\frac{\partial \mathbf{u}}{\partial t} + \mathbf{u}.\nabla\mathbf{u}\right) = -\nabla p + \mu_f\nabla^2\mathbf{u} + \rho_f g\beta(T_f - T_m) - \mathbf{S} \tag{2}$$

where $\mathbf{u}$ is the velocity vector (u, v, w), ρ_f is the fluid density, μ_f is the dynamic viscosity, $\nabla^2\mathbf{u}$ is the Laplacian of the velocity vector, and $\mathbf{S}$ is the source term vector (S_x, S_y, S_z) expressed as

$$\mathbf{S} = \frac{C(1-\lambda_l)^2}{\delta + \lambda_l{}^3} \tag{3}$$

The liquid fraction $\lambda_l$varies from 0 (complete solid) to 1 (complete liquid). The mushy zone parameter C was set to a FLUENT default value of 10^5 [27]. The modified Carman-Kozeny equation (Eq. 3) is derived from Darcy's law, which governs flow in porous media. The standard

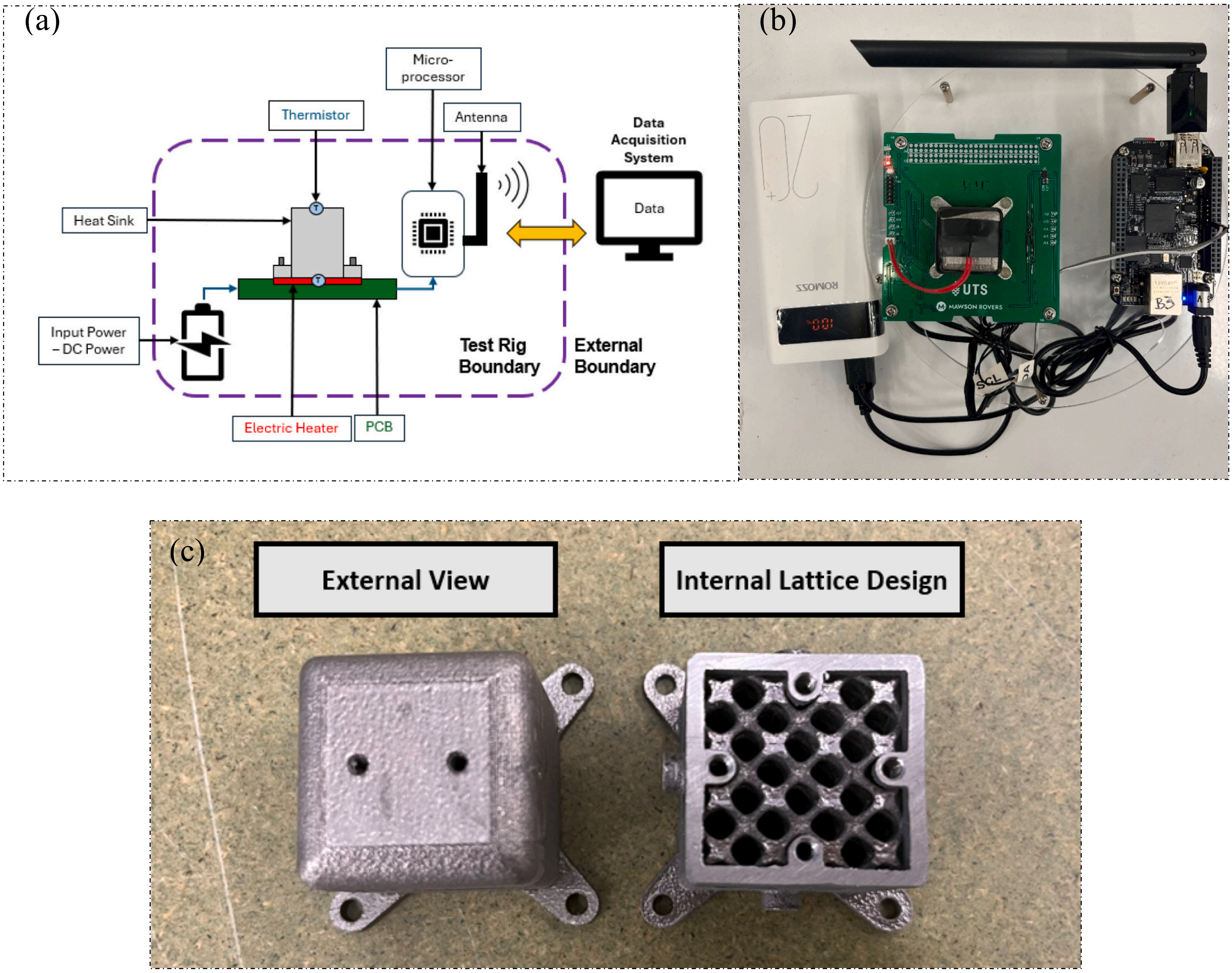

Fig. 4. Experimental set-up (a) 2-D schematic showing different components used in the experiment; (b) picture depicting actual PCB board, battery, sensors and a microprocessor; (c) actual prints of design P3.

Table 5
Variation of experimental tests.

Test variation	Material	PCM mass (g)	Heater power (W)			Ambient
A	Titanium	6	5.1	6.8	8.6	Atmosphere
B	Stainless Steel	6	5.1	6.8	8.6	Atmosphere

Carman-Kozeny equation returns an infinite value for **S** at zero liquid fraction; therefore, an arbitrary computational constant $\delta = 0.001$ is included in the modified equation [30]. The value of T_m in Eq. 2 represents the melting temperature of the PCM, which is the average of the solidus and liquidus temperatures of paraffin wax (55.5 °C).

Additionally, the energy equation for the PCM is as follows.

$$\rho_f C_{pf}\left(\frac{\partial T_f}{\partial t} + \mathbf{u}.\nabla T_f\right) = k_f \nabla^2 T_f - \rho_f L\,\frac{\partial \lambda_l}{\partial t} \tag{4}$$

The temperature-dependent liquid fraction is updated according to:

$$\lambda_l = \begin{cases} 0, & \text{if } T_f \leq T_{sol} \\ \dfrac{T_f - T_{sol}}{T_{liq} - T_{sol}}, & \text{if } T_{sol} \leq T_f \leq T_{liq} \\ 1, & \text{if } T_f \geq T_{liq} \end{cases} \tag{5}$$

where $C_{p,f}$ is the specific heat and k_f is the thermal conductivity of the PCM. For a solid material, the energy equation is reduced to unsteady heat conduction:

$$\rho_s C_{p,s}\left(\frac{\partial T_s}{\partial t}\right) = k_s \nabla^2 T_s \tag{6}$$

where ρ_s is the density of the solid, $C_{p,s}$ is the specific heat of the solid, and k_s is the thermal conductivity of the solid.

2.4. Initial and boundary conditions

The initial and boundary conditions of the simulation are illustrated in Fig. 2. The outside walls and top surface of the lid were set to convection boundary conditions with a heat transfer coefficient (HTC) modified to 40 W/m^{2}K to mimic the actual room conditions. A uniform heat-flux boundary was applied to the base of the heat sink to account

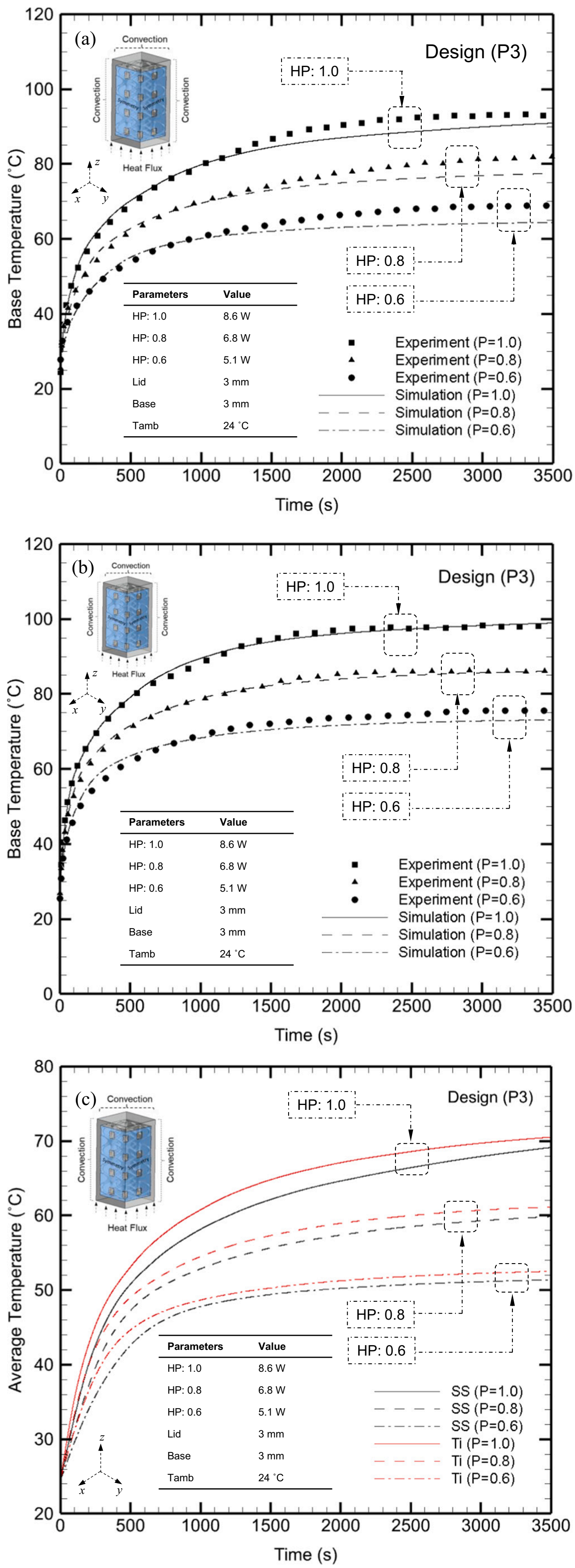

(caption on next column)

Fig. 5. (a) Base temperature evolution of the stainless-steel heat sink over time; (b) base temperature evolution of the titanium heat sink over time.; (c) volume-averaged temperature of the entire heat sink (metal + PCM) for both stainless steel and titanium heat sinks, providing a holistic comparison of thermal performance.

for the heat dissipated from the heater chip. The heat rejected from the PCB heater at full heater capacity was measured to be approximately 8.6 W (Heater Power:1.0) divided by the bottom wall surface area, which was considered to be the magnitude of the uniform heat flux applied to the base. The initial temperature for all the simulations was set to 24.5 °C and the initial velocity was assumed to be zero for all cases considered.

2.5. Grid independence and time step sensitivity analysis

An example of the mesh used in the calculation is shown in Fig. 2 (b). The mounting lugs, fillets, holes, and rounded corners were removed from the drawing prior to meshing to reduce the mesh size. A tetra/hexa mesh was converted into a polyhedral mesh to reduce the cell count and ensure the accuracy of the simulation. The mesh quality check was performed before initializing the solution, and only 1 % of the cells out of 2.1 M were found to be below 0.8 orthogonal quality. Grid independence analysis was conducted as one of the prerequisites of the CFD simulation. Five different grid sizes were considered to determine their effects on simulation accuracy, as shown in Fig. 3. The maximum variations in melting time and base temperature were 0.08 % and 0.1 %, respectively, as presented in Table 4. Grid 3 was deemed suitable for all simulations to obtain reasonable results with less computational time. Four different time steps (1.5, 1, 0.5 and 0.1 s were considered to obtain time-independent results. The maximum difference in temperatures and liquid fraction observed between time steps at equal physical times was <0.2 %, hence a time step of 0.5 s was found suitable for the results presented here.

3. Experiment

3.1. Setup

A heat sink was attached to a printed circuit board (PCB) equipped with an electric heater and thermistor. The thermistor was centrally positioned in the heated area of the PCB (Fig. 4(a)) and measures the base temperature of the heat sink at 5-s intervals during the heating process. The heat sink absorbs heat from the heater and transfers it to the PCM for storage. Temperature data collected by the thermistor were processed using a BeagleBone Black microprocessor and transmitted wirelessly to a web-based control dashboard. Both the PCB and microprocessor were powered by a battery. Fig. 4 shows a schematic and a photograph of the experimental setup. Tests were conducted for Cases 1–6 of Table 2. An organic solid-liquid PCM was selected owing to its uniform melting properties, chemical stability, and minimal volumetric change during the phase transition. Paraffin wax (Sigma-Aldrich 327204) with a melting point of 53 to 58 °C was chosen for its suitable operating properties.

The custom-made PCB featured a copper heater as a thermal power source. The heater area was 30 × 30 mm^2 at the PCB center, where the heat sink was mounted. A digital multimeter measured the heater resistance and voltage at ambient temperature, showing values of 2.3 Ω and 4.46 V, respectively. These measurements indicated a thermal power input of 8.6 W at full capacity. The measurement uncertainties were ± 1.5 % for resistance and ± 0.5 % for voltage. The NTCS0603E3103FMT thermistor manufactured by Vishay had a measurement uncertainty of ±1 %. The overall uncertainty in the thermal power input was calculated using the root sum square method and was found to be ±1.8 %. The detailed uncertainty analysis has been provided

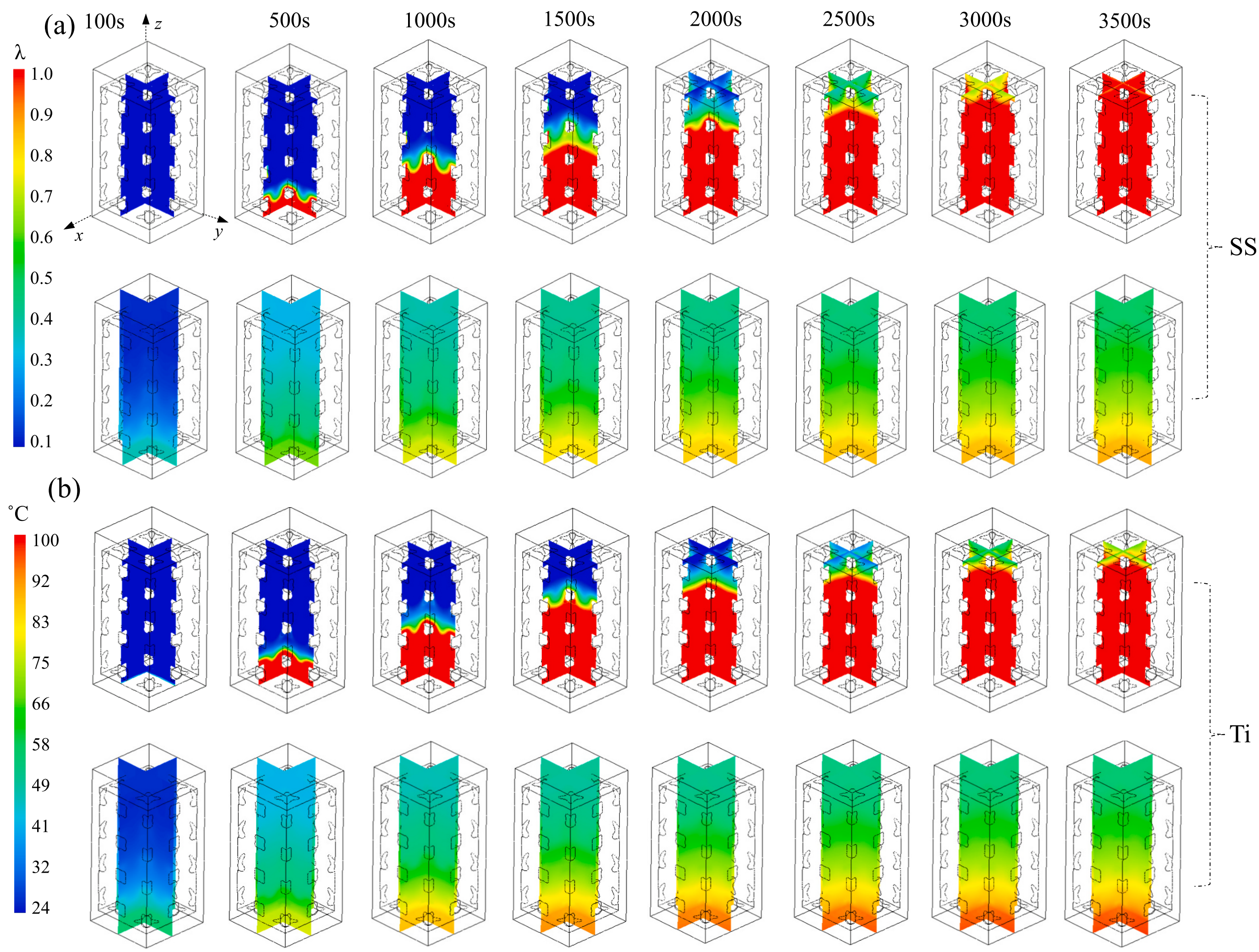

Fig. 6. Transient contours at full heater power (8.6 W) (a) liquid fraction and temperature profiles for stainless steel; (b) liquid fraction and temperature profiles for titanium.

in authors' previous work [36].

3.2. Test procedure

Two variations of the tests were performed, as shown in Table 5. All experiments were conducted in at power levels 0.6, 0.8 and 1.0 and comprised of 60 min of heating. At power level 1.0, the heater operates at full voltage (4.46 V), which translates to an initial power of 8.6 W. Power levels 0.8 and 0.6 are referent to 80 % and 60 % of the full voltage. Therefore, the initial power inputs of the experiments are 8.6 W for 1.0, 6.8 W for 0.8, and 5.1 W for 0.6. To evaluate the thermal performance of the heat sink, experiments were conducted with two heat sink materials: Titanium and Stainless Steel. The PCM experiments with variations A and B were repeated three times at each power level. The heat sink design proposed in this study is intended for thermal management in high-power electronic devices, such as CPUs, GPUs, and power converters, where typical heat dissipation ranges from 5 W to 100 W. The experimental power levels (5.1 W to 8.6 W) were selected to represent a subset of this range, focusing on low to medium power applications. These power levels are relevant to many practical scenarios, including portable electronics, embedded systems, and small-scale power electronics, where efficient heat dissipation is critical for maintaining device performance and durability. By evaluating the heat sink's performance within this range, the study provides insights that can be extended to higher power applications, ensuring the design's relevance to a wide array of electronic devices.

To conduct the PCM tests, liquid paraffin wax was injected into the heat sink via PCM injection openings on the top surface. The mass of the PCM was 6 g, which, when in its liquid form, occupied approximately half of the available internal volume. The heat sink was mounted on the PCB using nylon nuts and screws to prevent heat dissipation through screws via conduction. Additionally, a layer of Apiezon H thermal grease was applied between the heater and bottom surface of the heat sink to minimize the thermal contact resistance.

All experiments were conducted in a laboratory environment at standard room temperature and atmospheric pressure, and the same P3 heat-sink model was tested. The starting temperature of each test was maintained within tolerance 24 °C ± 0.5 °C. Thermal grease was evenly spread across the areas of contact with the heat sink to create a uniform heat-flux boundary as a control to obtain more accurate temperature measurements from the thermistors. A clock in the PCB design ensured that the temperature readings were taken at equal increments, and the heating cut-off time was programmed to maintain consistency between tests. Experiments were conducted inside a metal container with no lid to minimize the effect of ambient movements and isolate the test environment. The initial temperature setpoint for the bottom surface of the heat sink was 24 °C with the heater was turned off. Once the heater was switched on, the temperature at the base of the heat sink was monitored and measured at 5-s intervals until it reached 100 °C. After the heater was shut off, the temperature during cooldown was continuously

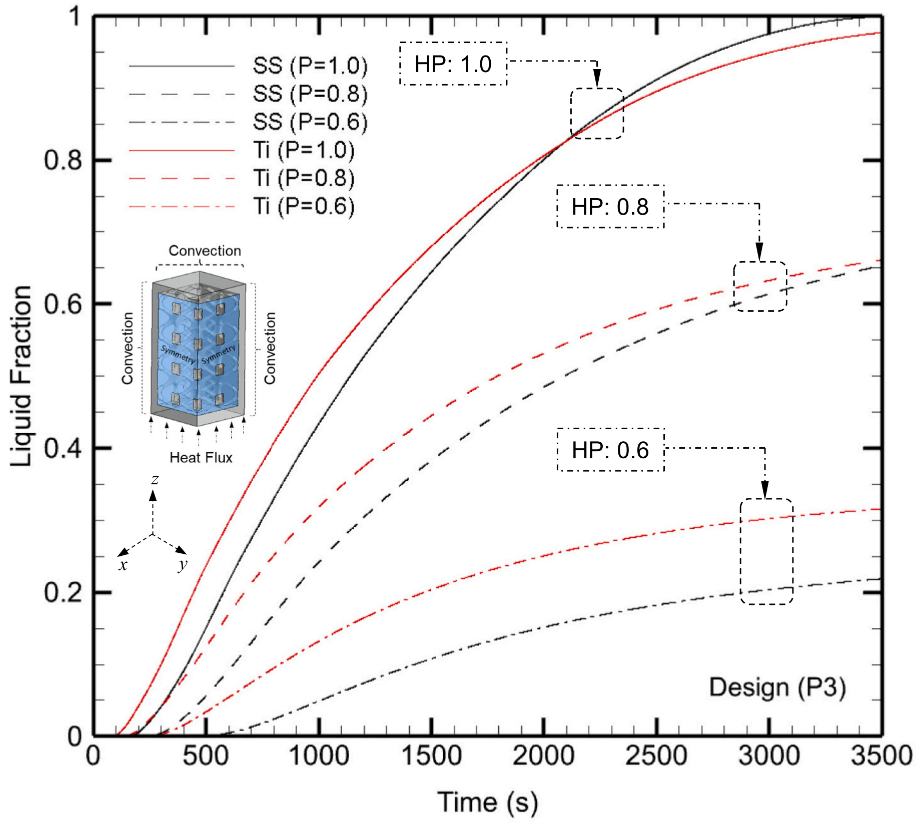

Fig. 7. Liquid fraction of stainless steel and titanium at all heater power inputs.

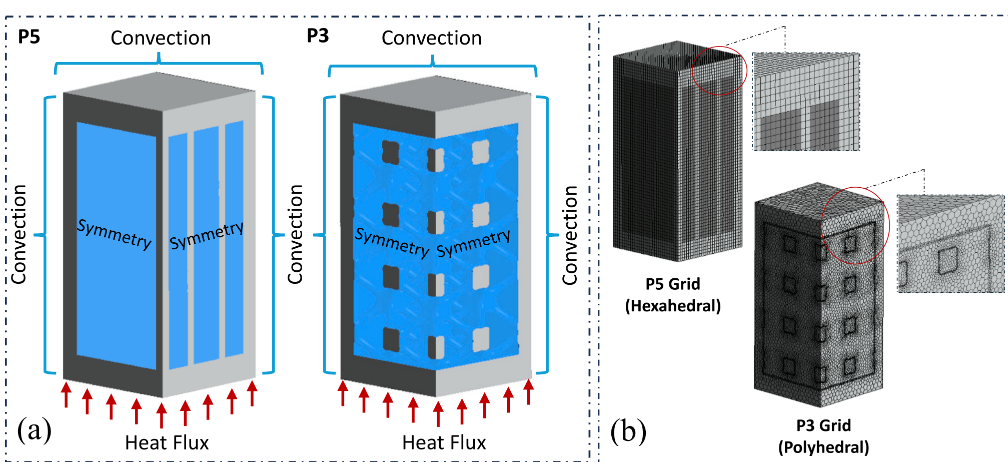

Fig. 8. P3 and P5 simulation models: (a) initial and boundary conditions; (b) computational grids.

monitored.

4. Results and discussion

This section presents the transient temperature profiles, liquid fraction visualizations, and thermal performance of the TPMS-based metal lattice heat sink (P3) and radial fin heat sink (P5) with phase change material (PCM). The results are analyzed to evaluate the impacts of key parameters, including material properties, heat power input, heat sink design, and heating direction (base, side, and combined heating). The discussion is structured to first examine the influence of material selection, followed by the effects of heat power, and finally the performance under different heating scenarios. This approach ensures a clear and logical progression, highlighting the relationships between the parameters and their collective impact on the thermal management of the heat sink.

4.1. *Effect of materials, heat power input on temperature and melting profiles*

The choice of material significantly influences the thermal performance of the heat sink. Stainless steel exhibits higher thermal conductivity (16.3 W/mK) compared to titanium (11.4 W/mK), resulting in more efficient heat transfer from the heat source to the PCM. This is evident in the lower base temperatures observed for the SS heat sink (Fig. 5a) compared to the titanium heat sink (Fig. 5b). Additionally, the

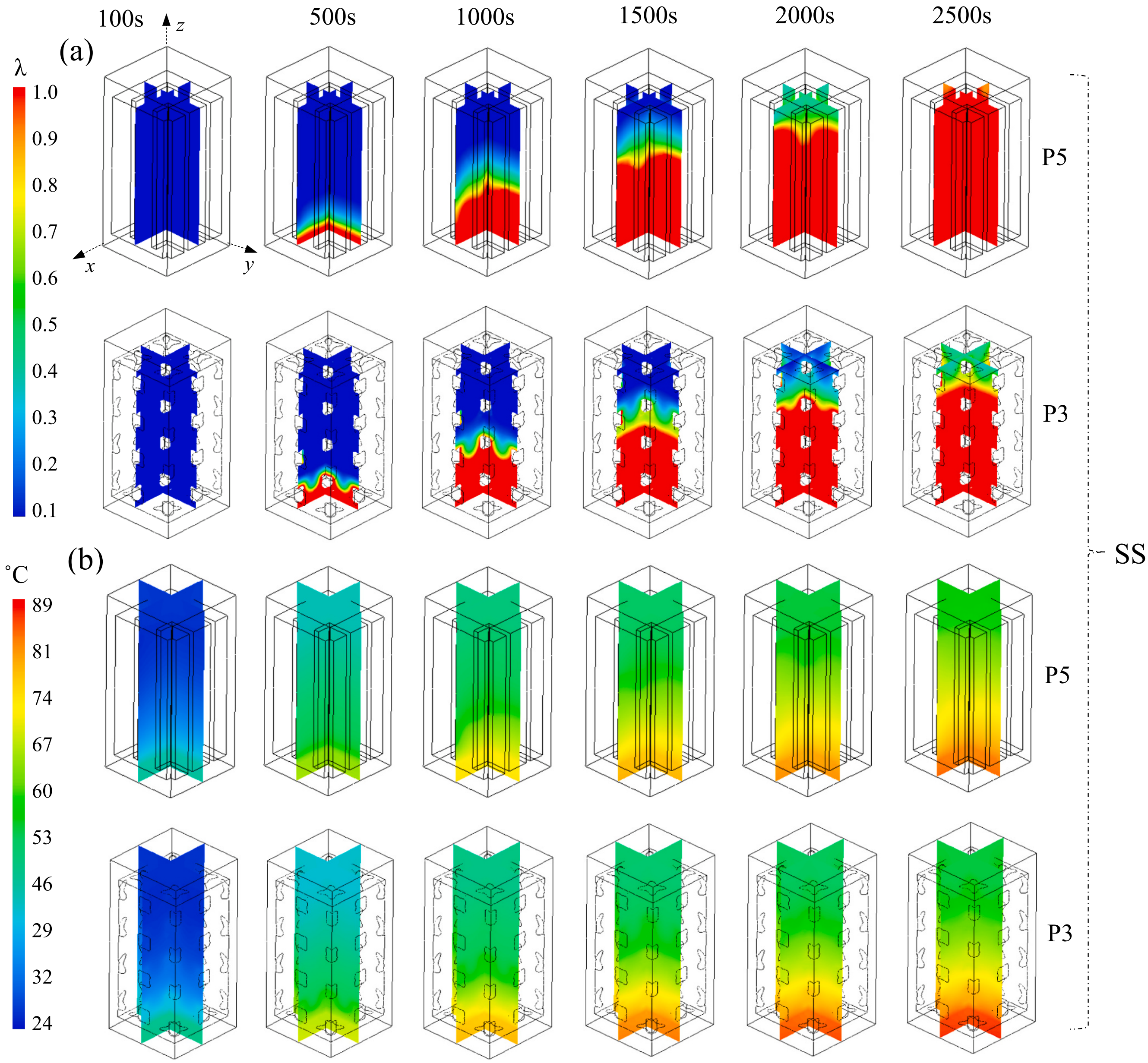

Fig. 9. Effect of base heating (a) liquid fraction; (b) average temperature.

higher specific heat capacity of titanium (544.25 J/kgK) compared to SS (502.5 J/kgK) means that titanium requires more energy to raise its temperature, which contributes to slower melting of the PCM in the later stages (Fig. 7). These findings highlight the importance of material selection in optimizing the thermal performance of PCM-based heat sinks.

The heat power input directly affects the rate of temperature rise and the melting behaviour of the PCM. At higher power inputs (8.6 W), the base temperature of the heat sink increases more rapidly, and the PCM melts faster due to the greater heat flux (Fig. 5). However, the effect of heat power is modulated by the material properties, as seen in the slower melting of the titanium heat sink compared to the stainless-steel heat sink at the same power input (Fig. 7). This interaction between heat power and material properties highlights the need to consider both factors when designing heat sinks for specific applications.

4.1.1. Temperature profiles

Fig. 5 (a) and (b) shows the experimental validation of the heat-sink base temperature for both stainless steel and titanium at different heat inputs ranging from 5.16 to 8.6 W. Initially, there is a steady rise in temperature for the heat sink in both materials due to the dominance of conduction heat transfer in the pre-sensible heating phase, with the heat being absorbed by the metal only. The base temperature reached 90 °C in approximately an hour for stainless steel, while the titanium heat sink reached to 98 °C at the same time. The more rapid rise in the base temperature for the titanium heat sink can be traced back to the lower thermal conductivity of the material (stainless steel conducts 1.4 times more heat than titanium). As observed in Fig. 5 (a) and (b), the use of the PCM in conjunction with the TPMS metal lattice results in a low and stable temperature rise for both heat sink materials at all power levels. For the stainless-steel heat sink, the base temperature reached a maximum of 90 °C at full heater power (8.6 W), 81 °C at 80 % heater power (6.8), and 69 °C at 60 % heater power, respectively. Similarly, for the titanium heat sink, the rise in temperature with different heat inputs was 98 °C, 86 °C, and 75 °C with decreasing power input, respectively. The same trend was observed in the simulation models, where the temperature rise with the materials and heat input were found to be consistent with the experiments.

The maximum temperature difference between the experiment and

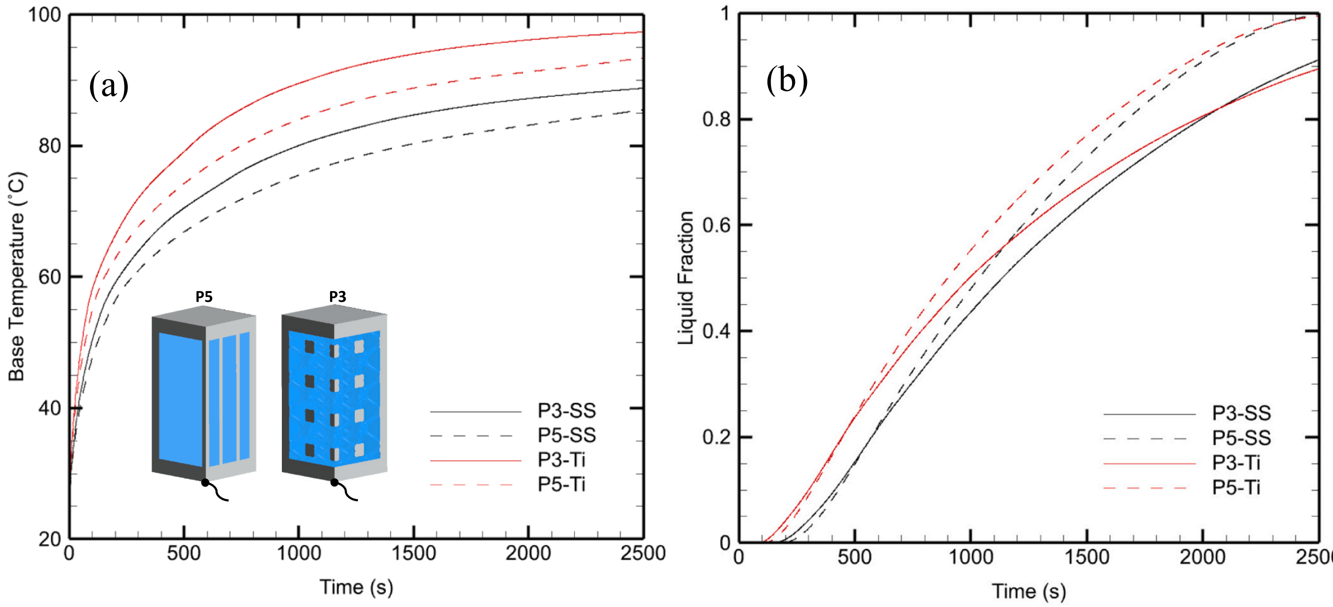

Fig. 10. Effect of base heating (a) base temperature with points of measurement (b) liquid fraction.

Table 6
Temperature and liquid fraction for design P3 and P5 at 2500 s.

Design	Material	Base temp (°C)	Liquid fraction (%)
P3	SS	88.7	0.91
P5	SS	85.4	0.99
P3	Ti	97.3	0.89
P5	Ti	93.3	0.99

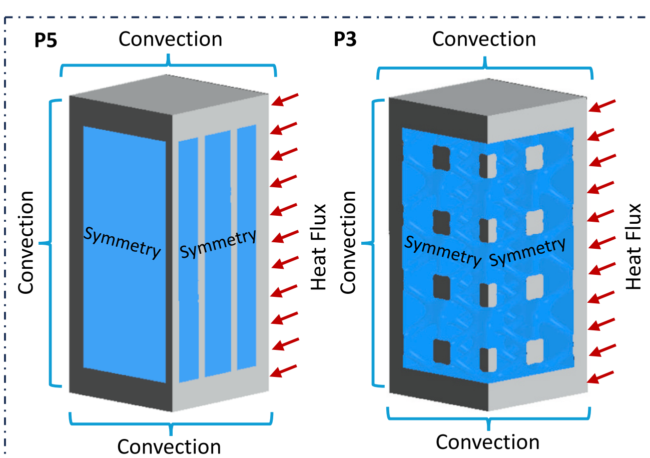

Fig. 11. Initial and boundary conditions for designs P5 and P3.

simulation results was 3.7 °C for stainless steel heat sink, while the difference was only found to be <2 °C for titanium heat sink. The differences can be attributed to variations in realized thermal conductivity of as-built parts and the air space at the top of the heat sink in the experiment. Additionally, a flattening of the temperature curve was observed for the heat sink with PCM in both cases, indicating melting of the PCM. As a result, continuous operation of the PCM-based heat sink is critical for its functionality as a TES system. Observing the volume average temperature of the PCM-embedded TPMS design (as shown in Fig. 5 (c)), one can see that titanium leads to a higher steady-state temperature rise for all heating inputs. The smooth and stable temperature rise in both materials shows the effectiveness of using PCM with a TPMS metal lattice structure as a thermal conductivity enhancer. The effect of the convective heat transfer coefficient on the overall thermal performance of the heat sink is also evident in keeping the temperatures low, even at full heater power input.

Another important point to consider is that the heat sink equipped with the PCM can maintain the base temperature at a lower level because the PCM has a much larger specific heat capacity (2000 J/kg. K) compared with air, which allows it to absorb a significant amount of heat per unit kg. This is supported by the numerical simulation results, which agree well with the experimental results in both cases (Fig. 5 (a) and (b)). However, the simulations did not account for the volume expansion of the PCM within the sink, resulting in a longer phase transition period and a larger amount of latent heat. The difference in having more PCM and no volume expansion in the simulation is evident in the stability of the temperature profiles because the heat exchange between the solid and liquid interface is through to the top and the unperturbed flow dynamics make the melting smooth. In the experiment, the smooth heat transfer is only up to the middle of the cavity before the volume expansion occurs, which eventually perturbs the flow dynamics and hence the base temperature profiles. However, the results shown in Fig. 5 do not include a post-sensible heating phase. Additionally, the higher thermal conductivity of stainless steel compared with titanium can explain the difference between the temperatures of the two samples.

4.1.2. *Melting profiles*

The inclusion of a TPMS-based metal lattice within the cavity and convection heat transfer to the outside have a substantial influence on the molten PCM flow dynamics and progression of the melt front, as depicted in Fig. 6. Initially, the PCM remained solid because all the heat supplied was used to increase the temperature of the metal until the system reached the melting point of the PCM. Once the heat penetrates through the solid via conduction, melting begins at the lattice-PCM interface and progresses towards the top, with more melting occurring along the cells. To aid in visualization, the liquid fraction and temperature profiles were extracted only in the x-z and y-z planes, as shown in Fig. 6. The x-z and y-z planes display the formation of Bernard convection cells due to bottom heating, which grows larger as melting progresses and moves towards the top along with the natural convection flow initiated by the lattice cells. As melting nears completion, the onset of strong natural convection flow patterns near the top suppressing

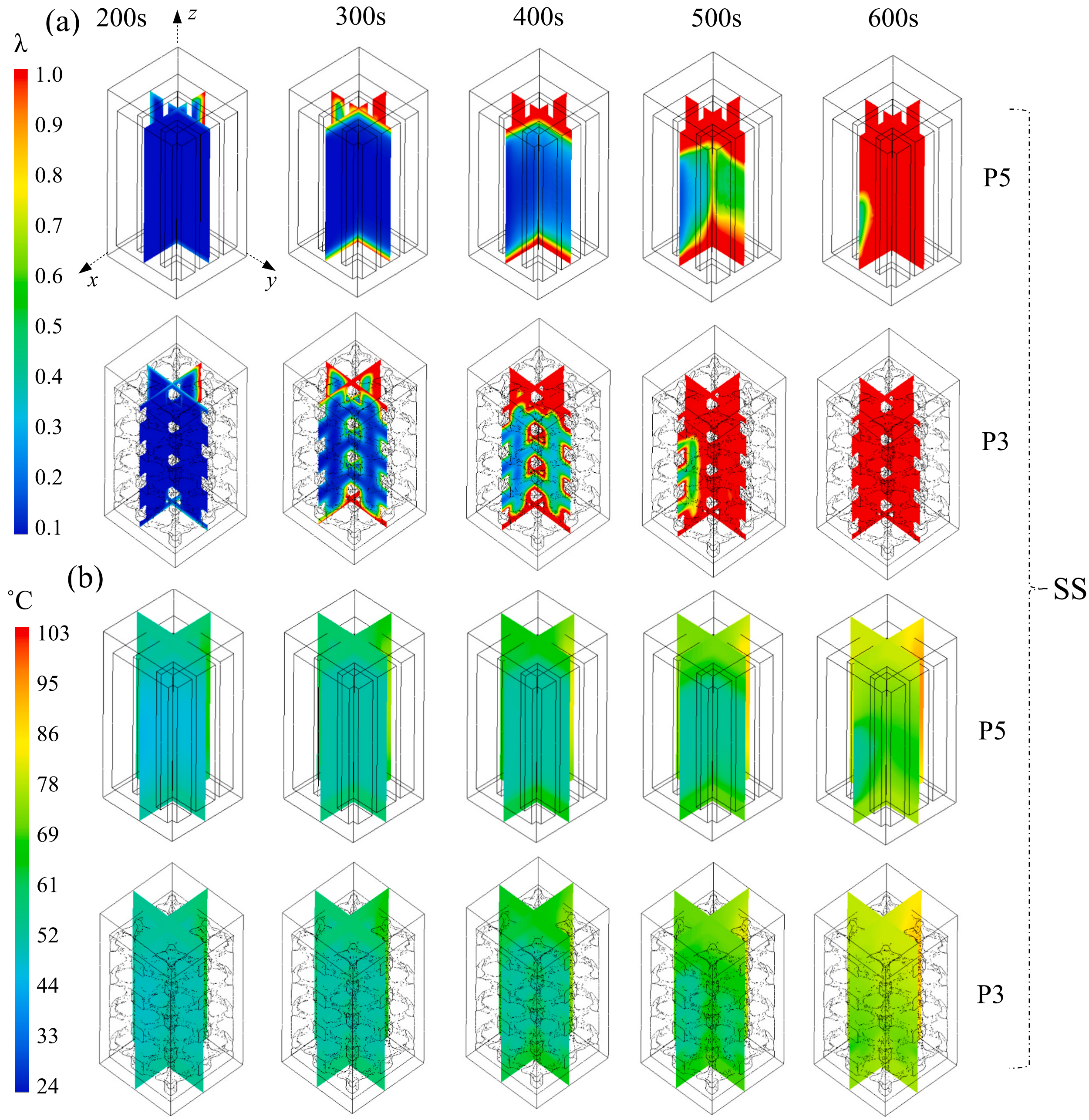

Fig. 12. Effect of side heating (a) liquid fraction; (b) average temperature.

Bernard cells, resulting in a smoother flow pattern. Thermal stratification is formed as the solid PCM melts at the top, and the formation of a wavy liquid fraction is partially due to the effect of buoyancy and wall heating when the hot PCM moves upward. The liquid PCM adjacent to the cell walls moves downward, resulting in a higher heat transfer rate near the walls and an inclined flow pattern. However, this pattern is not as strong for titanium (Fig. 6 (b)) because of the low thermal conductivity of the material and less heat exchange between the metal and PCM.

The presence of TPMS-based lattice structure inside the cavity resulted in a smoother and unperturbed flow pattern, as evidenced by the x-z and y-z planes. The heat exchange at the lattice-PCM interface generates a pair of convection cells that move in the vertical direction, promoting faster melting at the solid-liquid interface. The porosity of the structure accelerated the movement of these patterns and caused the PCM to melt more rapidly. It is evident from Fig. 6 that the convective flow near the cells has a stronger impact than that near the walls because of the external wall heat transfer to the surroundings in both planes. Fig. 6 also illustrates the transient temperature profiles of the heat sink during physical melting. As melting progresses, the heat sink's base and average temperature increase towards 100 °C at 3500 s, with titanium being the hotter. The velocity streamlines of the melted PCM inside the heat sink are not shown here; however, as melting progresses, the velocity of the molten PCM increases, reaching a maximum upon complete melting.

Fig. 7 depicts the liquid fractions of stainless steel and titanium at all heater power inputs. As can be seen, the rapid initial melting of the titanium heat sink can be attributed to the lower specific heat capacity of titanium compared to stainless steel, which allows it to heat up more quickly in the early stages. However, as the melting progresses, the lower thermal conductivity of titanium becomes a limiting factor, slowing down the heat transfer to the PCM and resulting in slower melting in the later stages. The turning point at 2000 s is due to the transition from conduction-dominated heat transfer (initial phase) to

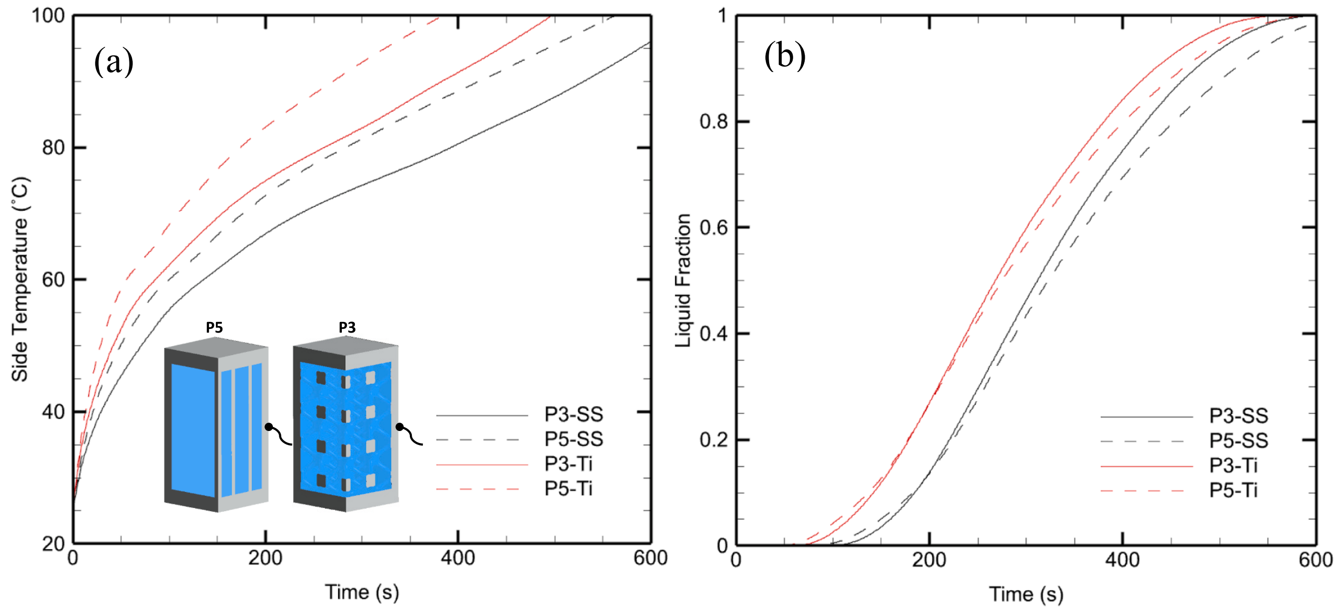

Fig. 13. Effect of side heating (a) side temperature with points of measurement (b) liquid fraction.

Table 7
Temperature and liquid fraction for design P3 and P5 at 600 s.

Design	Material	Side temp (°C)	Liquid fraction (%)
P3	SS	96.0	0.99
P5	SS	102.6	0.98
P3	Ti	110.7	1.0
P5	Ti	118.1	1.0

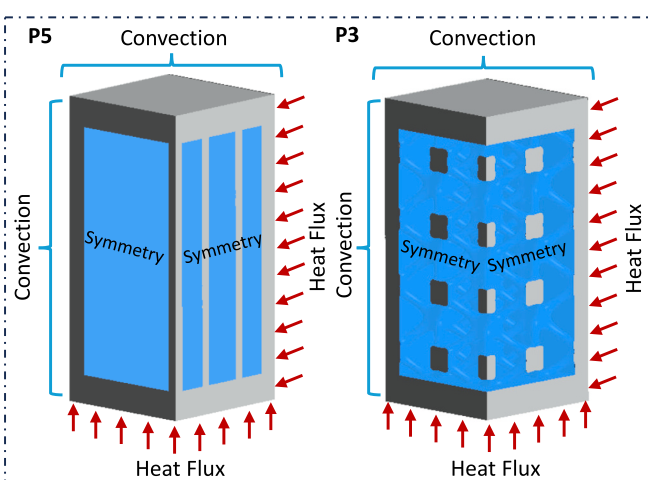

Fig. 14. Initial and boundary conditions for design P5 and P3.

convection-dominated heat transfer (later phase), where the thermal conductivity of the material plays a more significant role. The difference in melting increased as the heat input decreased, as depicted in Fig. 7, with 65 % melting performed at 80 % heater power and 32 % at 60 % for the titanium heat sink model.

4.2. *Effect of base heating*

The effect of base heating on the performance of the P3 and P5 heat sinks with stainless steel and titanium materials is illustrated in Fig. 8–10. Two designs, one with radial fins and the other with a TPMS-based metal lattice as thermal conductivity enhancers, were compared to assess the effectiveness of the internal structure in terms of keeping the electronics cool at a constant heater power input. Two identical domains, in terms of mass and external dimensions, were considered for the analysis, as shown in Fig. 8, along with the boundary conditions and computational grids. Because design P5 is considerably simpler than design P3, a hexahedral grid with proper refinement is considered. As expected, the results indicate that for base heating, design P5 with radial fins attached to the base is more effective in keeping the base cooler than design P3 with the TPMS metal lattice, as depicted in Table 6 and Fig. 10 for both stainless steel and titanium. The reason for this is that in the radial fin design, the extended surfaces are only attached to the base where the heat is supplied, and the fins help take the heat quickly to the top with a quicker exchange between the solid and liquid interfaces in the direction of the supplied heat. However, in the TPMS design, owing to the symmetrical lattice structure in each direction, the heat exchange between the lattice and PCM occurs gradually, leading to slower melting, as depicted in Fig. 9. The complete melting of the PCM occurred in approximately 2500 s in design P5, whereas the melting took approximately 3500 s in the lattice design. Design P5 is 1.4 times effective than design P3 in the base-only heating case. From Fig. 10 and Table 6, it can be observed that for stainless steel heat sink designs, P5 maintains a base 3 °C cooler than P3, while this difference is noted to be 4 °C for titanium heat sinks.

4.3. *Effect of side heating*

One can consider a scenario in which heat is transferred to the heat sink from the sides, such as in a confined space where airflow is limited. To simulate this, the impact of side heating on the performance of the P3 and P5 heat sinks with stainless steel and titanium materials is illustrated in Figs. 11–13. The initial and boundary conditions along the heating wall are shown in Fig. 11. The results indicate that for side wall heating, the design with radial fins is less effective in keeping the side wall cooler than the lattice structure. The reason for this is that in the design with a TPMS-based metal lattice, the cells are attached to the wall, which helps in solid-solid (conduction) and solid-liquid (convection) heat exchange within the cavity quickly as compared to that of the design with radial fins, where the fins are only attached to the bottom wall. Owing to the absence of a solid TCE attached to the side wall in the radial fin design, the exchange only occurs at the solid-liquid interface

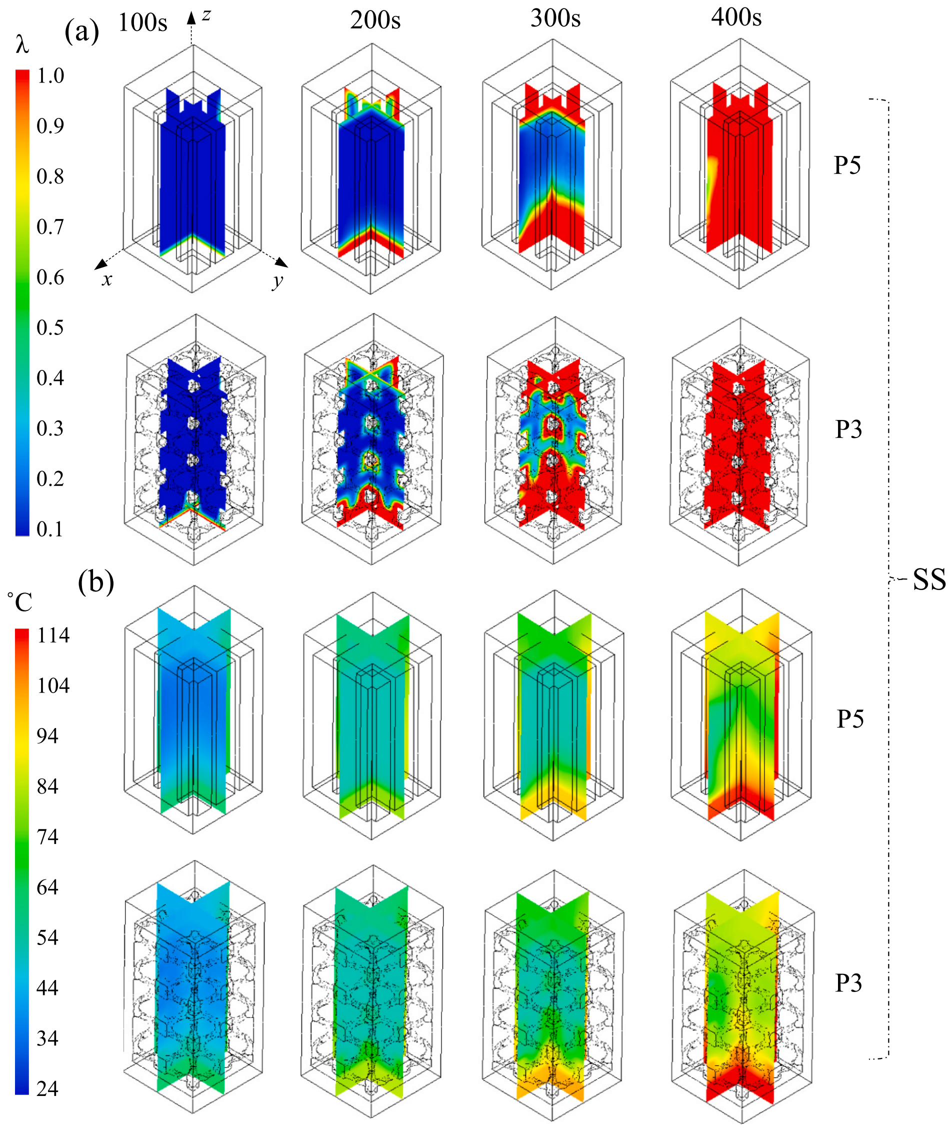

Fig. 15. Effect of base and side heating (a) liquid fraction; (b) average temperature.

once it passes through the solid wall. The area between the wall and the subsequent fin acts as a cavity with only the PCM inside, and the poor thermal conductivity of the PCM slows the melting process, unlike TPMS TPMS-based metal lattice heat sink. Fig. 12 shows the transient contours of the liquid fraction and average volume temperatures for both designs in the stainless-steel material. It can be observed that at 600 s, all the PCM inside the TPMS-based metal lattice heat sink is melted with the side temperature reaching 96 °C, whereas the radial fin design shows slow melting with the side temperature reaching 102 °C. The sidewall temperature difference between the two designs is noted to be 6 °C for stainless steel and 8 °C for titanium, as shown in Table 7 and Fig. 13.

4.4. Combined effect of base and side heating

One can also consider a scenario in which there is a combination of upward and lateral heat transfers, such as in a confined space with heat sources at various orientations. To simulate this, the impact of base and side wall heating on the performance of P3 and P5 heat sinks of stainless steel and titanium is illustrated in Figs. 14–16. The initial and boundary conditions along with the heating walls are depicted in Fig. 14. The results indicate that for base and side heating, both designs perform similarly, with P3 being slightly better at maintaining the average temperature of the base side lower in the case of stainless steel, while there is almost no change observed in titanium. It was envisaged that the effect of vertical fins in design P5 diluted the effect of slow melting through the sides, whereas in P3, the symmetrical lattice structure on each side explains the melting process. The transient contours of the liquid fraction and volume average temperature are presented in Fig. 15 for stainless steel heat sinks, where a slightly slower melting in design P5 can be visualized at 400 s. It should be noted that the designs considered here are identical in terms of weight and external physical dimensions, and the average volume temperature for both designs and materials is found to be similar as well. The vertex average temperatures of the base and side walls at 400 s along with the liquid fraction are listed in Table 8 and presented in Fig. 16, where the transient temperature and melting profiles are captured for both designs and materials at a constant heater power input (8.6 W) from the base and side walls. It is important to note that the temperature profiles presented in Fig. 16 (a) represent the average temperature of the base and side, rather than the volume-averaged temperature of the entire heat sink. The localized over-heating observed before 400 s is attributed to the high thermal conductivity of the metal lattice, which facilitates rapid heat conduction away from the heat source. Due to the lower thermal conductivity of PCM, heat diffusion is slower within the domain, causing a temperature

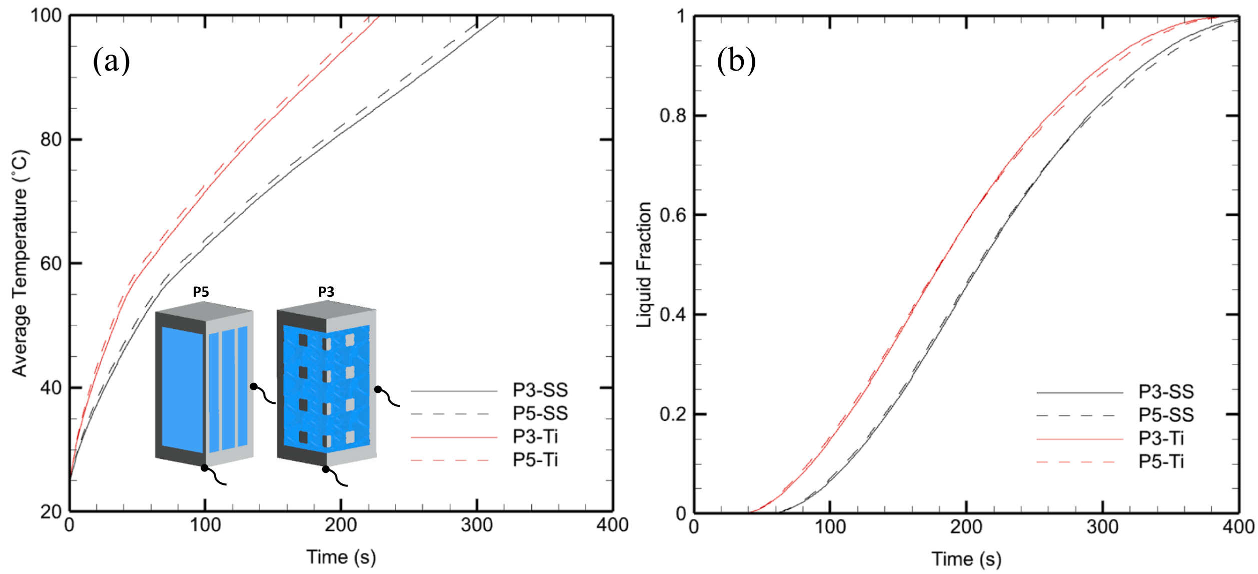

Fig. 16. Effect of base and side heating (a) average temperature of points of measurement; (b) liquid fraction.

Table 8
Temperature and liquid fraction for design P3 and P5 at 400 s.

Design	Material	Avg. temp (°C)	Liquid fraction (%)
P3	SS	113.8	0.99
P5	SS	114.6	0.99
P3	Ti	134.3	1.0
P5	Ti	134.3	0.99

Table 9
Summary table.

Parameter	Effect on temperature	Effect on melting time	Key observation
Material (SS vs. Ti)	SS maintains lower base temp	SS melts faster than Ti	Higher thermal conductivity of SS improves heat transfer and melting efficiency.
Heat Power (5.1–8.6 W)	Higher power → higher temp	Higher power → faster melt	Heat power directly influences temperature rise and melting rate.
Base Heating	P5 outperforms P3	P5 melts faster than P3	Radial fins (P5) enhance heat transfer under base-only heating.
Side Heating	P3 outperforms P5	P3 melts faster than P5	TPMS lattice (P3) improves heat dissipation under side-only heating.
Base + Side Heating	Minimal difference between P3 and P5	Similar melting times	Combined heating reduces the performance gap between P3 and P5.

difference between the metal and PCM regions. This results in localized temperature peaks exceeding 100 °C while portions of the PCM are still undergoing phase change. The overlapping insets in Fig. 16 (a) show the temperature measurement locations. Table 9 summarizes the key findings for each parameter (material, heat power, and heating direction) and their influence on the base temperature, melting time, and overall thermal performance of the heat sink.

5. Conclusions and future recommendation

This study provides a comprehensive numerical and experimental analysis of a TPMS-based metal lattice heat sink with the aim of enhancing the thermal performance of modern electronics. This study examines the effectiveness of using a metal lattice as a TCE in conjunction with PCM. In addition, a parametric study was conducted to investigate the influence of different materials, power inputs, designs, and multidirectional heating on the overall cooling performance. Based on the findings, the following conclusions were drawn.

1. The effect of the heat sink material is significant. The stainless-steel heat sink was found to be better in terms of maintaining a base temperature lower than titanium due to its lower thermal conductivity. The reduction in base temperature for stainless steel at full heater power (8.6 W) was 9 %, while this difference decreased with decreasing power input by 6 % at 6.8 W and 8.6 % at 5.1 W heater power, respectively.
2. The liquid fraction simulations support the hypothesis that with more heater power input and better thermal conductivity, melting occurs more rapidly inside the heat sink. At full heater power, 100 % PCM melts in approximately 3500 s for SS (P3), while 98 % melting is achieved for Ti (P3) for the same amount of time.
3. For base-only heating, the choice of heat sink structure was found to be significant. The radial fin design (P5) was more effective than with the TPMS-based metal lattice (P3), and the SS (P5) base temperature was found to be 3 °C lower than that of SS(P3). This difference was noted to be 4 °C for Ti (P5) and Ti (P3) designs.
4. The effect of side heating was found to be significant when compared the two designs. Design P3 with a metal lattice structure outperformed the radial fin design by keeping the wall 6 °C cooler for stainless steel and 8 °C for titanium.
5. For combined base and side heating the choice of heat sink structure was found to be insignificant, as the results showed a very slight change in vertex average temperature for both designs and materials.

This study provides valuable insights for design engineers and researchers by explaining the influence of geometry, materials, and the direction of applied heat input on the selection of optimal heat sink designs for thermal management in power electronics. This is particularly relevant for applications involving multidirectional heat dissipation. While stainless steel and titanium were chosen for their widespread use in additive manufacturing and their contrasting thermal properties, future studies could explore the use of aluminium and its alloys. Aluminium alloys, with their superior thermal conductivity and lower cost, present a promising alternative for cost-sensitive applications, especially in environments where high-temperature and corrosive resistance are less critical. Further research could evaluate the performance of aluminium-based TPMS structures in comparison to stainless steel and titanium, offering insights into applications that demand both thermal efficiency and cost-effectiveness. Additionally, extending the power range to higher levels (e.g., up to 100 W) would allow for the evaluation of the heat sink's performance under more demanding conditions, broadening its applicability to a wider range of electronic devices. Future recommendations also include investigating advanced TPMS-based metal lattice structures with enhanced thermal conductivity, combined with innovative phase change materials such as nano-enhanced PCMs (Ne-PCMs), to further improve thermal management solutions.

CRediT authorship contribution statement

Mohammad Arqam: Writing – review & editing, Writing – original draft, Visualization, Validation, Software, Methodology, Conceptualization. **Laryssa Sueza Raffa:** Writing – review & editing, Writing – original draft, Validation, Data curation. **Simone Spisiak:** Writing – review & editing, Formal analysis, Data curation. **Lee Clemon:** Writing – review & editing, Supervision, Resources, Project administration. **Zhen Luo:** Writing – review & editing, Resources, Project administration, Funding acquisition. **Matt Ryall:** Writing – review & editing, Resources, Project administration, Funding acquisition. **Mohammad S. Islam:** Writing – review & editing, Project administration, Funding acquisition. **Nick S. Bennett:** Writing – review & editing, Supervision, Resources, Project administration, Funding acquisition.

Declaration of competing interest

The authors declare that they have no known competing financial interests or personal relationships that could have affected the research presented in this study.

Acknowledgement

The SmartSat Cooperative Research Council and the University of Technology Sydney (UTS) jointly funded this study, with additional support provided by Romar Engineering Pty. Ltd. for the 3D printing of heat sinks. The UTS and high-performance computing facilities were utilized for experimental work and numerical modelling, respectively.

Data availability

Data will be made available on request.

References

[1] S.M.S. Murshed, C.A. Nieto de Castro, A critical review of traditional and emerging techniques and fluids for electronics cooling, Renew. Sust. Energ. Rev. 78 (2017) 821–833.
[2] K. Du, J. Calautit, Z. Wang, Y. Wu, H. Liu, A review of the applications of phase change materials in cooling, heating, and power generation in different temperature ranges, Appl. Energy 220 (2018) 242–273.
[3] K. Hosseinzadeh, M.A. Erfani Moghaddam, A. Asadi, A.R. Mogharrebi, D.D. Ganji, Effect of internal fins along with hybrid nanoparticles on solid process in star shape triplex latent heat thermal energy storage system by numerical simulation, Renew. Energy 154 (2020) 497–507.
[4] K. Hosseinzadeh, M.A. Erfani Moghaddam, A. Asadi, A.R. Mogharrebi, B. Jafari, M. R. Hasani, D.D. Ganji, Effect of two different fins (longitudinal-tree like) and hybrid nanoparticles (MoS2-TiO2) on solidification process in triplex latent heat thermal energy storage system, Alex. Eng. J. 60 (1) (2021) 1967–1979.
[5] K. Hosseinzadeh, E. Montazer, M.B. Shafii, A.R.D. Ganji, Solidification enhancement in triplex thermal energy storage system via triplets fins configuration and hybrid nanoparticles, Journal of Energy Storage 34 (2021) 102177.
[6] A. Arshad, M. Jabbal, Y. Yan, Thermal performance of PCM-based heat sink with partially filled copper oxide coated metal-foam for thermal management of microelectronics, in: 2020 19th IEEE Intersociety Conference on Thermal and Thermomechanical Phenomena in Electronic Systems (ITherm), IEEE, 2020, pp. 1–8.
[7] Q. Ren, Z. Wang, J. Zhu, Z.G. Qu, Pore-scale heat transfer of heat sink filled with stacked 2D metal fiber-PCM composite, Int. J. Therm. Sci. 161 (2021) 106739.
[8] Q. Ren, Z. Wang, T. Lai, J.F. Zhang, Z.G. Qu, Conjugate heat transfer in anisotropic woven metal fiber-phase change material composite, Appl. Therm. Eng. 189 (2021) 116618.
[9] Q. Ren, P. Guo, J. Zhu, Thermal management of electronic devices using pin-fin based cascade microencapsulated PCM/expanded graphite composite, Int. J. Heat Mass Transf. 149 (2020) 119199.
[10] J. Chen, D. Yang, J. Jiang, A. Ma, D. Song, Research progress of phase change materials (PCMs) embedded with metal foam (a review), Procedia Mater. Sci. 4 (2014) 389–394.
[11] A. Chamkha, A. Veismoradi, M. Ghalambaz, P. Talebizadehsardari, Phase change heat transfer in an L-shape heatsink occupied with paraffin-copper metal foam, Appl. Therm. Eng. 177 (2020) 115493.
[12] M. Ghalambaz, J. Zhang, Conjugate solid-liquid phase change heat transfer in heatsink filled with phase change material-metal foam, Int. J. Heat Mass Transf. 146 (2020) 118832.
[13] M. Kibria, M. Anisur, M. Mahfuz, R. Saidur, I. Metselaar, A review on thermophysical properties of nanoparticle dispersed phase change materials, Energy Convers. Manag. 95 (2015).
[14] K.Y. Leong, M.R.A. Rahman, B.A. Gurunathan, Nano-enhanced phase change materials: a review of thermo-physical properties, applications, and challenges, Journal of Energy Storage 21 (2019) 18–31.
[15] C. Ho, Y.-C. Liu, M. Ghalambaz, W.-M. Yan, Forced convection heat transfer of nano-encapsulated phase change material (NEPCM) suspension in a mini-channel heatsink, Int. J. Heat Mass Transf. 155 (2020) 119858.
[16] S.E. Awan, M. Awais, M.A.Z. Raja, N. Parveen, H.M. Ali, W.U. Khan, Y. He, Numerical treatment for dynamics of second law analysis and magnetic induction effects on ciliary induced peristaltic transport of hybrid nanomaterial, Front. Phys. 9 (2021) 68.
[17] M.A. Khan, M.K. Imam, K. Irshad, H.M. Ali, M.A. Hasan, S. Islam, Comparative overview of the performance of cementitious and non-cementitious nanomaterials in mortar at normal and elevated temperatures, Nanomaterials 11 (4) (2021) 911.
[18] M. Ghaneifar, A. Raisi, H.M. Ali, P. Talebizadehsardari, Mixed convection heat transfer of Al2O3 nanofluid in a horizontal channel subjected with two heat sources, J. Therm. Anal. Calorim. 143 (3) (2021) 2761–2774.
[19] W. Usman, W. Khan, I.A. Badruddin, A. Ghaffari, H.M. Ali, Heat transfer in steady slip flow of tangent hyperbolic fluid over the lubricated surface of a stretchable rotatory disk, Case Studies in Thermal Engineering 24 (2021) 100825.
[20] H. Ji, D.P. Sellan, M.T. Pettes, X. Kong, J. Ji, L. Shi, R.S. Ruoff, Enhanced thermal conductivity of phase change materials with ultrathin-graphite foams for thermal energy storage, Energy Environ. Sci. 7 (3) (2014) 1185–1192.
[21] T. Kim, D. Singh, W. Zhao, W. Yua, D.M. France, An investigation on the effects of phase change material on material components used for high temperature thermal energy storage system, in: AIP Conference Proceedings vol. 1734, No. 1, AIP publishing, 2016, May.
[22] Z. Yu, D. Feng, Y. Feng, X. Zhang, Thermal conductivity and energy storage capacity enhancement and bottleneck of shape-stabilized phase change composites with graphene foam and carbon nanotubes, Compos. A: Appl. Sci. Manuf. 152 (2022) 106703.
[23] J.Y. Ho, K.C. Leong, Experimental investigation of a PCM-based topology optimized heat sink for passive cooling of electronics, in: Heat Transfer Summer Conference, American Society of Mechanical Engineers, 2020.
[24] G. Yuandong, Y. Huning, L. Guiping, J. Haichuan, S. Xiaobin, M. Jianyin, Thermal performance of a 3D printed lattice-structure heat sink packaging phase change material, Chin. J. Aeronaut. 34 (5) (2021) 373–385.
[25] X. Hu, X. Gong, Experimental study on the thermal response of PCM-based heat sink using structured porous material fabricated by 3D printing, Case Studies in Thermal Engineering 24 (2021) 100844.
[26] G. Righetti, G. Savio, R. Meneghello, L. Doretti, S. Mancin, Experimental study of phase change material (PCM) embedded in 3D periodic structures realized via additive manufacturing, Int. J. Therm. Sci. 153 (2020) 106376.
[27] A.-C. Iradukunda, A. Vargas, D. Huitink, D. Lohan, Transient thermal performance using phase change material integrated topology optimized heat sinks, Appl. Therm. Eng. 179 (2020) 115723.
[28] S. Catchpole-Smith, R. Selo, A. Davis, I. Ashcroft, C. Tuck, A. Clare, Thermal conductivity of TPMS lattice structures manufactured via laser powder bed fusion, Addit. Manuf. 30 (2019) 100846.
[29] Z.A. Qureshi, S.A.B. Al Omari, E. Elnajjar, F. Mahmoud, O. Al-Ketan, R.A. Al-Rub, Thermal characterization of 3D-printed lattices based on triply periodic minimal surfaces embedded with organic phase change material, Case Studies in Thermal Engineering 27 (2021) 101315.
[30] R.R. Selo, S. Catchpole-Smith, I. Maskery, I. Ashcroft, C. Tuck, On the thermal conductivity of AlSi10Mg and lattice structures made by laser powder bed fusion, Addit. Manuf. 34 (2020) 101214.
[31] Z.A. Qureshi, S.A.B. Al-Omari, E. Elnajjar, O. Al-Ketan, R.A. Al-Rub, Using triply periodic minimal surfaces (TPMS)-based metal foams structures as skeleton for metal-foam-PCM composites for thermal energy storage and energy management applications, International Communications in Heat and Mass Transfer 124 (2021) 105265.
[32] Z.A. Qureshi, E. Elnajjar, O. Al-Ketan, R.A. Al-Rub, Heat transfer performance of a finned metal foam-phase change material (FMF-PCM) system incorporating triply periodic minimal surfaces (TPMS), Int. J. Heat Mass Transf. 170 (2021) 121001.

[33] Z.A. Qureshi, S.A.B. Al-Omari, E. Elnajjar, O. Al-Ketan, R.A. Al-Rub, Nature-inspired triply periodic minimal surface-based structures in sheet and solid configurations for performance enhancement of a low-thermal-conductivity phase-change material for latent-heat thermal-energy-storage applications, Int. J. Therm. Sci. 173 (2022) 107361.

[34] Z.A. Qureshi, S.A.B. Al-Omari, E. Elnajjar, O. Al-Ketan, R.A. Al-Rub, On the effect of porosity and functional grading of 3D printable triply periodic minimal surface (TPMS) based architected lattices embedded with a phase change material, Int. J. Heat Mass Transf. 183 (2022) 122111.

[35] M. Arqam, L.S. Raffa, L. Clemon, M.S. Islam, M. Ryall, N.S. Bennett, Numerical and experimental investigation of a phase change material radial fin heat sink for electronics cooling, Journal of Energy Storage 98 (2024) 113113.

[36] L.S. Raffa, M. Ryall, N.S. Bennett, L. Clemon, Experimental investigation of the performance of a phase change material thermal management module under vacuum and atmospheric pressure conditions, Int. J. Heat Mass Transf. 236 (2025) 126384.

[37] X. Hu, X. Gong, F. Zhu, X. Xing, Z. Li, X. Zhang, Thermal analysis and optimization of metal foam PCM-based heat sink for thermal management of electronic devices, Renew. Energy 212 (2023) 227–237.

[38] A. Arshad, M. Jabbal, P. Talebizadeh Sardari, M.A. Bashir, H. Faraji, Y. Yan, Transient simulation of finned heat sinks embedded with PCM for electronics cooling, Thermal Science and Engineering Progress 18 (2020) 100520.

[39] K.C. Nayak, S.K. Saha, K. Srinivasan, P. Dutta, A numerical model for heat sinks with phase change materials and thermal conductivity enhancers, Int. J. Heat Mass Transf. 49 (11−12) (2006) 1833–1844.

[40] H. Yang, Y. Li, L. Zhang, Y. Zhu, Thermal performance enhancement of phase change material heat sinks for thermal management of electronic devices under constant and intermittent power loads, Int. J. Heat Mass Transf. 181 (2021) 121899.

[41] A. Abdi, V. Martin, J.N.W. Chiu, Numerical investigation of melting in a cavity with vertically oriented fins, Appl. Energy 235 (2019) 1027–1040.